On the eddy viscosity formulation in large-eddy simulation wall models

By X. I. A. Yang

1. Motivation and objectives

Wall-bounded flows are often encountered in engineering and geophysical applications. A robust feature of wall-bounded flows is the presence of the logarithmic region, where neither the viscous effects nor the large-scale boundary effects are dynamically important (Marusic *et al.* 2013). At low speeds (for constant property flows), the mean flow follows the logarithmic law of the wall in the logarithmic region

$$U^+ = 1/\kappa \ \log(y^+) + B, \tag{1.1}$$

where U is the mean streamwise velocity, y is the distance from the wall, $+$ indicates normalization by wall units, κ is the von Kármán constant and B is an additive constant. The size of the smallest eddies in wall-bounded flows scale with ν/u_τ, where ν is the kinematic viscosity, $u_\tau = \sqrt{\tau_w/\rho}$ is the friction velocity, τ_w is the mean wall-shear stress and ρ is the fluid density. Unless otherwise noted all quantities in this paper are ensemble averaged mean quantities. At high Reynolds numbers, directly resolving such small-scale eddies is computationally costly (Choi & Moin 2012), and a common practice is to model the near-wall turbulence using a wall model (Piomelli & Balaras 2002; Piomelli 2008; Park 2017). In the context of large-eddy simulations (LES), the most commonly used wall model is the so-called equilibrium wall model (Kawai & Larsson 2012; Larsson *et al.* 2016)

$$\frac{d}{dy}\left[(\mu + \mu_{t,wm})\,\frac{du_{||}}{dy}\right] = 0, \tag{1.2}$$

$$\frac{d}{dy}\left[(\mu + \mu_{t,wm})\,u_{||}\frac{du_{||}}{dy} + c_p\left(\frac{\mu}{\mathrm{Pr}} + \frac{\mu_{t,wm}}{\mathrm{Pr}_{t,wm}}\right)\frac{dT}{dy}\right] = 0, \tag{1.3}$$

where the two Reynolds-Averaged-Navier-Stokes-type equations are numerically integrated on a one-dimensional grid in the near-wall region (to a wall-normal distance h_{wm} from the wall, where the solution matches with the LES), and the resulting wall-shear stress and wall heat transfer rate are fed to LES as boundary conditions (see Figure 1). Here $u_{||}$ is the instantaneous wall-parallel velocity, T is the instantaneous temperature, μ is the instantaneous dynamic viscosity, Pr is the Prandtl number, c_p is the specific heat, μ_t is the instantaneous eddy viscosity, Pr_t is the turbulent Prandtl number and the subscript wm denotes quantities used in a wall model (as opposed to LES quantities). We use x, y and z for the streamwise, wall-normal and spanwise directions, respectively. u, v, w and U, V, W are used for the instantaneous and the mean velocity in the three Cartesian directions. The eddy viscosity $\mu_{t,wm}$ may be specified using the mixing length model (Pope 2001)

$$\mu_{t,wm} = \sqrt{\rho\rho_w}\kappa u_\tau y \cdot D, \tag{1.4}$$

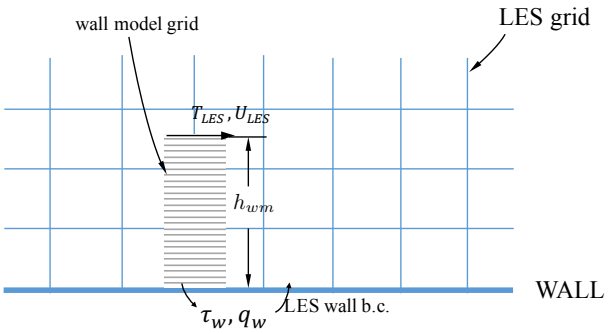

FIGURE 1. Schematics of wall-modeled large-eddy simulation (WMLES). The LES grid cannot resolve all near-wall eddies. Equations (1.2), (1.3) are solved on the embedded wall model grid, with the instantaneous LES temperature T_{LES} and LES velocity U_{LES} as matching conditions at a distance h_{wm} from the wall. The resulting wall-shear stress τ_w and wall heat transfer rate q_w are fed to LES as boundary conditions for integrating the LES equations. Here, b.c. is short for boundary condition.

where D is the van Driest damping function

$$D = \left[1 - \exp\left(-y^+/A^+\right)\right]^2. \tag{1.5}$$

Here $A^+ = 17$ is a model constant and subscript w indicates quantities at the wall. This work focuses on the functional behavior of the eddy viscosity, which is not necessarily used in an LES wall model, hereafter, we will refer to $\mu_{t,wm}$ (generally) as μ_t. The turbulent Prandtl number is $\mathrm{Pr}_t = 0.9$. The non-equilibrium terms including the unsteady term, the wall-parallel convective terms $u\partial u/\partial x$ and $w\partial u/\partial z$ and the pressure gradient term are dropped in Eqs. (1.2), (1.3) (the reader is directed to Yang *et al.* (2015); Yang & Bose (2017); Park & Moin (2014) for wall models that account for these non-equilibrium effects explicitly). Despite this apparent shortfall, the model has been quite useful for capturing wall-shear stresses and wall heat transfer rates in practically relevant flows both at low speeds (see, e.g., Yang & Meneveau 2016; Kawai & Asada 2013) and at high speeds (see, e.g., Bermejo-Moreno *et al.* 2014, 2011).

In this work, we focus on the specification of the damping function D for WM-LES of high-speed flows. We show that the conventional viscous scaling for y, i.e., $y^+ = y\sqrt{\rho_w\tau_w}/\mu_w$, is inappropriate for flows at high speeds (variable property flows), and instead, the semi-local scaling, i.e., $y_{SL} = y\sqrt{\rho\tau_w}/\mu$, must be used in the damping function D. Since D is part of the eddy viscosity μ_t, we will also investigate the behavior of μ_t.

By definition, the eddy viscosity μ_t is

$$\mu_t = \frac{\tau_w}{dU/dy} \tag{1.6}$$

in the logarithmic range, where we have neglected the molecular viscosity. At low speeds, dU/dy may be evaluated according to Eq. (1.1). At high speeds, the mean flow no longer follows the incompressible law of the wall, unless a velocity transformation is applied. The most commonly used velocity transformation is the so-called van Driest transformation (van Driest 2003)

$$\frac{dU^+_{VD}}{dU^+} = \sqrt{\frac{\rho_w}{\rho}}, \quad \frac{dY^+_{VD}}{dy^+} = 1, \tag{1.7}$$

where VD indicates van Driest transformed quantities, and the mean density ρ is a function of the wall-normal distance. Equation (1.7) works quite well for boundary-layer flows above adiabatic walls (where $d\mu/dy \approx 0$ in the viscous sublayer) (see, e.g., Pirozzoli & Bernardini 2013; Guarini *et al.* 2000; Martín 2007). For non-adiabatic walls, the van Driest transformation fails (Coleman *et al.* 1995; Foysi *et al.* 2004), and the velocity transformation by Trettel & Larsson (2016) must be used

$$\frac{dU_{TL}}{dU}\frac{dy}{dy_{TL}} = \frac{\mu}{\mu_w}, \quad y^+_{TL} = \frac{\sqrt{\rho\tau_w}}{\mu}y, \tag{1.8}$$

where TL indicates transformed quantities, and both μ and ρ are functions of the wall-normal distance. dU/dy in Eq. (1.6) can be evaluated according to

$$\frac{dU}{dy} = \frac{dU}{dU_T}\frac{dY_T}{dy}\frac{dU_T}{dY_T} = \frac{dU}{dU_T}\frac{dY_T}{dy}\frac{u_\tau}{\kappa Y_T}, \tag{1.9}$$

in the logarithmic region, where U_T and Y_T are the transformed velocity and wall-normal coordinate, $U_T(Y_T)$ follows the logarithmic law of the wall and $dU_T/dY_T = u_\tau/(\kappa Y_T)$, dU/dU_T and dY_T/dy are known when given a velocity transformation (Eq. (1.7) or Eq. (1.8)). Using Eqs. (1.6), (1.9), both the van Driest transformation (Eq. (1.7)) and the Trettel-Larsson transformation (Eq. (1.8)) lead to the same eddy viscosity

$$\mu_t = \sqrt{\rho\rho_w}\kappa u_\tau y, \tag{1.10}$$

in the logarithmic region (where the damping function is $D \approx 1$).

Following the van Driest transformation, y^+ measures the viscous distance from the wall, and the damping function Eq. (1.5) must be used. However, according to the Trettel-Larsson transformation, the viscous distance from the wall is measured using $y^+_{TL} = y\sqrt{\rho\tau_w}/\mu$ and the damping function must be

$$D = \left[1 - \exp(-y^+_{TL}/A^+)\right]^2. \tag{1.11}$$

We use y_{SL} and y^+_{TL} interchangeably. The subscript SL is short for "semi-local" (Huang *et al.* 1995; Patel *et al.* 2015, 2016).

The usefulness of Eq. (1.5) and Eq. (1.11) may be tested by solving directly Eqs. (1.2), (1.3) and comparing the transformed velocities with the incompressible law of the wall. Consistency requires that the transformed velocity follow the incompressible law of the wall. The results are shown in Figures 2 and 3. The ideal gas law $P = \rho RT$ is invoked, where R is the ideal gas constant. The specific heat is $c_p = \gamma/(\gamma - 1) \cdot R$, where the adiabatic index $\gamma = 1.4$. The molecular Prandtl number is Pr= 0.72, and $\kappa = 0.4$. The molecular dynamic viscosity is only a function of the temperature $\mu/\mu_{\text{ref}} = (T/T_{\text{ref}})^{0.7}$, where T_{ref} is a reference temperature. $T_w = 1$ is kept constant. The pressure is y-independent, and we set $P_{\text{LES}} = 1$. As a result, the sound speed at the wall is $a_w = 1$. The one-dimensional domain extends [0, 1], i.e., $h_{wm} = 1$. We use h_{wm}, a_w and T_w for normalization. The dynamic viscosity at the wall is $\mu_w = 1.0 \times 10^{-4}$. The velocity at $y = h_{wm}$ is kept constant at $U_{\text{LES}} = 2$, and we vary the fluid temperature at $y = h_{wm}$: $T_{\text{LES}} = 0.2$ [Figure 2(a), Figure 3(a)], $T_{\text{LES}} = 1$ [Figure 2(b), Figure 3(b)], and $T_{\text{LES}} = 5$ [Figure 2(c), Figure 3(c)] for different levels of wall heating. For the results shown in Figure 2, the conventional damping function Eq. (1.5) is used, and for the results in Figure 3, we have used Eq. (1.11). Using Eq. (1.5) (consistent with the van Driest transformation), U_{VD} do not collapse with the law of the wall. On the other hand, when Eq. (1.11) is used (following the Trettel-Larsson transformation), the

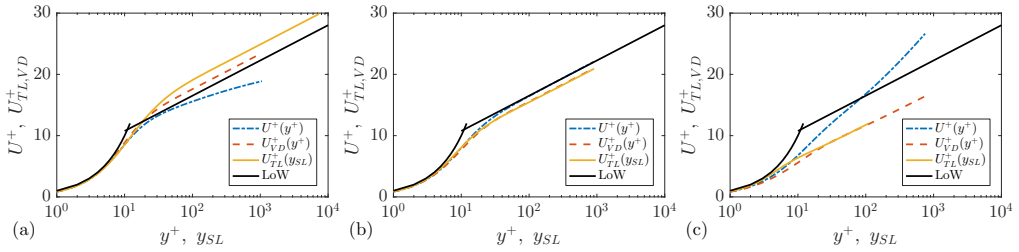

FIGURE 2. Solutions to Eqs. (1.2) and (1.3). Transformed and untransformed velocities as functions of the transformed and untransformed wall-normal distance. The damping function is specified according to Eq. (1.5). $T_w = 1$ and $\mu_w = 1 \times 10^{-4}$. (a) $T_{LES} = 0.2$. (b) $T_{LES} = 1$. (c) $T_{LES} = 5$.

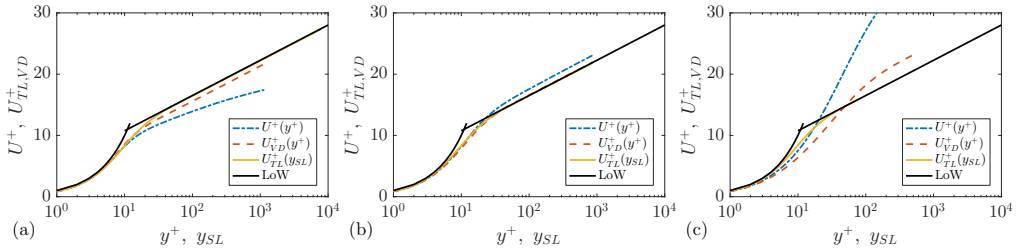

FIGURE 3. Same as Figure 2, but using Eq. (1.11) as the damping function. LoW stands for law of the wall, which comprises of a linear region and a logarithmic region.

transformed velocities follow closely the law of the wall. The latter is not surprising considering the fact that the Trettel-Larsson transformation was derived by equating the turbulent momentum flux and the viscous stress with their incompressible counterparts (see detailed discussion in Trettel & Larsson 2016). In all, this exercise brings to our attention the internal inconsistency of the van Driest transformation and the resulting eddy viscosity. In addition, the results in figures 2 and 3 favor (albeit by construction) Eq. (1.11).

We use direct numerical simulation (DNS) of supersonic Couette flow to test the usefulness of the eddy viscosity formulation Eq. (1.10) in the context of high speed flows. Since a mean pressure gradient is absent in Couette flow, Eqs. (1.2), (1.3) are good approximations of the flow near the wall, providing a good ground for testing the eddy viscosity formulation. As will be shown, the eddy viscosity does follow Eq. (1.10) in the logarithmic range. We will also test the usefulness of Eq. (1.5) and Eq. (1.11). The rest of the paper is organized as follows. The computational setup is briefly summarized in Section 2. The results are presented in Section 3, followed by conclusions in Section 4.

2. Computational setup

We use the unstructured, finite-volume compressible solver CharLES (Khalighi *et al.* 2011; Bermejo-Moreno *et al.* 2014). This code has been extensively used and validated for wall-bounded flow calculations (see, e.g., Larsson *et al.* 2015; Joo *et al.* 2014; Park 2017; Bermejo-Moreno *et al.* 2014). The code solves the Favre-filtered compressible Navier-Stokes equations for the conserved flow quantities of mass, momentum and total energy. We use the same constitutive equations as for the wall model equation; these have already been summarized in Section 1. For LES calculations, the eddy viscosity is modeled using

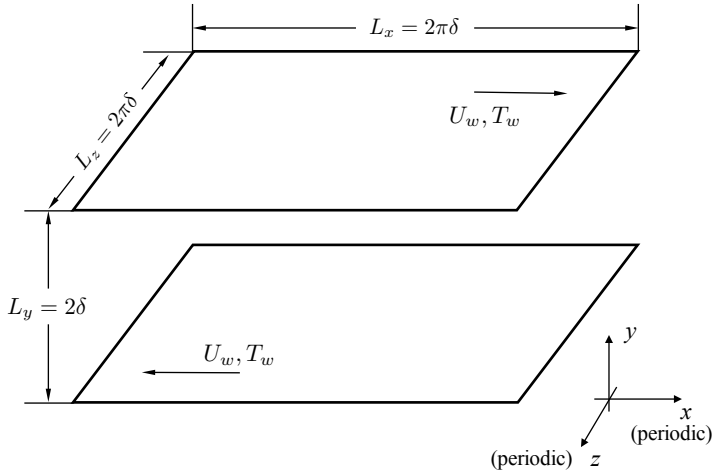

FIGURE 4. Schematics of the computational setup. x, y and z are the streamwise, wall-normal and spanwise directions, respectively. The two walls move at the same speed but in opposite directions. Both walls are isothermal and are kept at the same temperature. Periodic boundary conditions are imposed in both the x and z directions, and the no-slip condition is imposed on both walls.

the dynamic Vreman model (You & Moin 2007). A fourth-order central scheme is used for flux reconstruction in regions away from shocks. Shocks are detected using a Ducros shock sensor (Ducros *et al.* 1999; Bhagatwala & Lele 2009). Near shocks (at high speeds, shocklets form within the channel), an essentially non-oscillatory (ENO) scheme is used. A third-order explicit Runge-Kutta scheme is used for time integration.

The computational domain is sketched in Figure 4. Periodic boundary conditions are imposed in the streamwise and spanwise directions. The two walls are isothermal and are kept at the same temperature $T_w = 1$. The sound speed at the two walls is $a_w = 1$. The computational domain has dimensions $L_x \times L_y \times L_z = 2\pi\delta \times 2\delta \times 2\pi\delta$ in the streamwise, wall-normal and spanwise directions, respectively, where $\delta = 1$ is the half channel height. We use the sound speed at the wall, the half channel height and the wall temperature for normalization purposes.

A structured Cartesian grid with uniform grid spacing in the streamwise and spanwise directions is used for all calculations. Details of the DNS and WMLES are summarized in table 1. DNS of Couette flows at two wall Mach numbers, $M_w = 3$ and 6, are conducted. WMLES of the same flows are conducted using both damping functions formulations [i.e., Eq. (1.5) and Eq. (1.11)]. Grid convergence is shown for WMLES. For WMLES, the grid spacings Δ_x, Δ_y and Δ_z and the LES/wall-model matching height h_{wm} are such that $\Delta_x/h_{wm} = \Delta_z/h_{wm} = 0.63$ and $\Delta_y/h_{wm} = 0.4$, following Larsson *et al.* (2016).

Table 1 shows grid spacing in wall units. The typical grid resolution requirement for a channel flow is $\Delta_x^+ \approx 10$, $\Delta_{y,w}^+ \approx 0.5$, $\Delta_{y,c} \approx 6$, $\Delta_z^+ \approx 6$ (see, e.g., Hoyas & Jiménez 2006; Lozano-Durán & Jiménez 2014; Lee & Moser 2015), where w and c indicate quantities evaluated at the wall and at the channel center line. According to the above criterion, D-M3 is well resolved, but D-M6 is poorly resolved. However, viscous scaling defined at the wall is not very useful for examining the grid resolution at high speeds, and it is more meaningful to use local quantities (Huang *et al.* 1995)

$$u_{\tau,SL} = \sqrt{\tau_w/\rho}, \quad \delta_{\nu,SL} = \mu/u_{\tau,SL}, \tag{2.1}$$

Case	D	M_w	μ_w	$N_x \times N_y \times N_z$	$\Delta_x^+ \times \Delta_y^+ \times \Delta_z^+$	τ_w	Re_τ^*
D-M3	N/A	3.0	5.0e-4	$256 \times 185 \times 384$	$11 \times (0.19, 7.8) \times 7.6$	0.024	160
D-M6	N/A	6.0	1.0e-3	$256 \times 185 \times 384$	$17 \times (0.3, 12) \times 12$	0.11	100
W-M3$_{\mathrm{VD,c}}$	Eq. (1.5)	3.0	5.0e-4	$48 \times 24 \times 48$	$78 \times 50 \times 78$	0.039	207
W-M3$_{\mathrm{SL,c}}$	Eq. (1.11)	3.0	5.0e-4	$48 \times 24 \times 48$	$63 \times 40 \times 63$	0.025	170
W-M3$_{\mathrm{VD,f}}$	Eq. (1.5)	3.0	5.0e-4	$72 \times 36 \times 72$	$52 \times 33 \times 52$	0.038	205
W-M3$_{\mathrm{SL,f}}$	Eq. (1.11)	3.0	5.0e-4	$72 \times 36 \times 72$	$43 \times 27 \times 43$	0.025	170
W-M6$_{\mathrm{VD}}$	Eq. (1.5)	6.0	1.0e-3	$72 \times 36 \times 72$	$93 \times 60 \times 93$	0.22	109
W-M6$_{\mathrm{SL}}$	Eq. (1.11)	6.0	1.0e-3	$72 \times 36 \times 72$	$73 \times 47 \times 73$	0.11	88
W-hRe$_{\mathrm{VD}}$	Eq. (1.5)	3.0	1.0e-5	$72 \times 36 \times 72$	$1.8e3 \times 1.1e3 \times 1.8e3$	0.017	6.74e3
W-hRe$_{\mathrm{SL}}$	Eq. (1.11)	3.0	1.0e-5	$72 \times 36 \times 72$	$1.5e3 \times 9.6e2 \times 1.5e3$	0.012	5.95e3

TABLE 1. Details of the DNS and WMLES cases. Entries beginning with "D" are DNS cases, and Entries beginning with "W" are WMLES cases. c and f indicate coarse grid and fine grid. D is the wall damping. VD and SL refers to Eq. (1.5) and Eq. (1.11). M_w is the wall Mach number. τ_w is the wall-shear stress. μ_w is the wall dynamic viscosity. eX is $\times 10^X$. We have listed the smallest and the largest Δ_y^+ for the case D-M3 and the case D-M6, which correspond to the near-wall resolution and the resolution at the channel center line. $Re_\tau^* = \delta\sqrt{\rho_c \tau_w}/\mu_c$ is the friction Reynolds number defined using local quantities. Here c indicates quantities at the channel center line.

both of which are functions of the wall-normal distance. Figure 5(a) shows the grid resolution as functions of y_{SL}. At $y_{SL} = 5$ (i.e., within the viscous sublayer), the grid resolution of D-M3 is $\Delta_x/\delta_{\nu,SL} \approx 7.0$, $\Delta_y/\delta_{\nu,SL} \approx 0.8$ and $\Delta_z/\delta_{\nu,SL} \approx 4.7$, whereas the grid resolution of D-M6 is $\Delta_x/\delta_{\nu,SL} \approx 4.6$, $\Delta_y/\delta_{\nu,SL} \approx 0.7$ and $\Delta_z/\delta_{\nu,SL} \approx 3.1$. We therefore conclude that both DNS are well resolved. Figure 5 (b) shows $y_{SL} = y/\delta_{\nu,SL}$ as a function of y^+. For both DNS, $Re_\tau^* = \delta\sqrt{\tau_w \rho_c}/\mu_c < Re_\tau = \delta\sqrt{\tau_w \rho_w}/\mu_w$. In addition, D-M6 is at a lower Reynolds number than D-M3 using Re_τ^* (this is also clear from Figure 6).

3. Results

Figure 6 shows the instantaneous contours of the streamwise velocity on a spanwise-wall-normal plane at an arbitrarily chosen x location from D-M3 and D-M6. D-M3 is at a friction Reynolds number $Re_\tau^* = 160$ and D-M6 is at a friction Reynolds number $Re_\tau^* = 100$. As a result, the flow in D-M3 appears to contain more scales than the flow in D-M6.

Equation (1.10), i.e., the eddy viscosity used in wall models, is derived by assuming that the transformed velocity (using the van Driest transformation or the Trettel-Larsson transformation) collapses with the incompressible law of the wall. Here, we first test the usefulness of the two velocity transformations. Figure 7(a) shows the untransformed and transformed mean velocity profiles as functions of y^+ and y_{SL}. The transformed velocity using the Trettel-Larsson transformation follows closely the law of the wall, and the van Driest transformation fails to collapse the transformed velocity with Eq. (1.1). Because the eddy viscosity Eq. (1.10) may be derived using both the van Driest transformation and the Trettel-Larsson transformation, the results in Figure 7 at least shows that Eq.

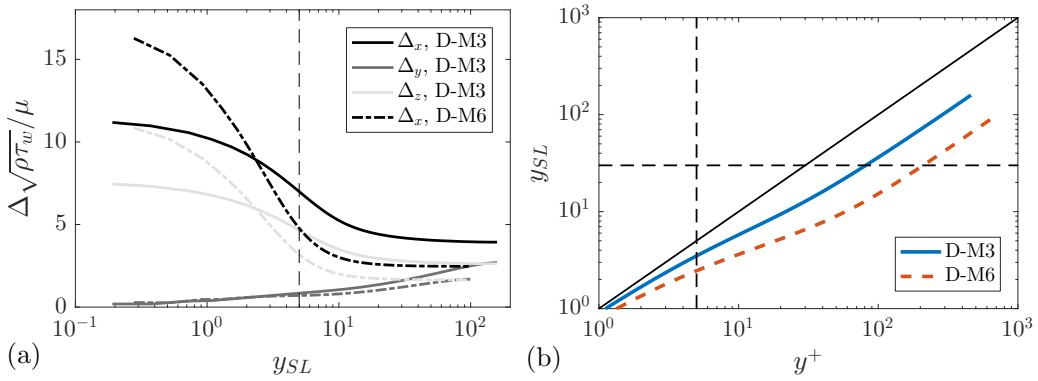

FIGURE 5. (a) Grid resolution $\Delta\sqrt{\rho\tau_w}/\mu$ as functions of y_{SL}. Resolutions in different Cartesian directions are gray-level-coded. We have used solid lines for D-M3 and dashed lines for D-M6. (b) $y_{SL} = y/\delta_{\nu,SL}$ as a function of y^+ for the two DNS cases. The thin solid line corresponds to the incompressible limit $y_{SL} = y^+$ (strictly speaking, the constant-property limit). The two dashed lines are at $y^+ = 5$ and $y_{SL} = 30$.

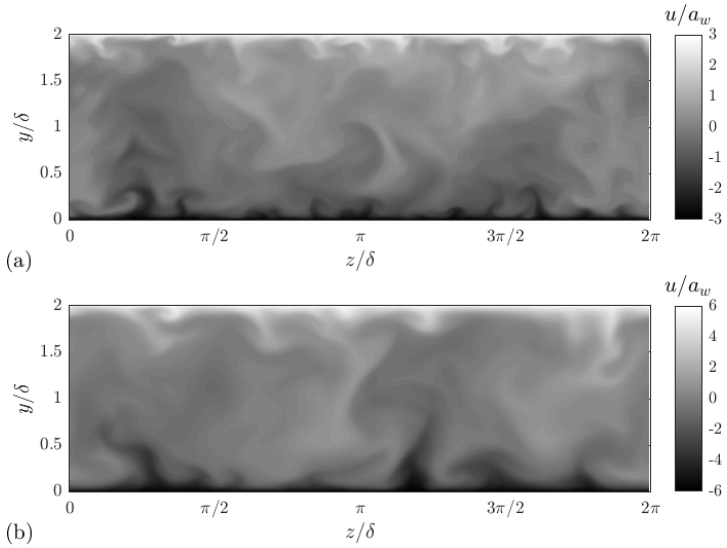

FIGURE 6. Instantaneous streamwise velocity on a spanwise-wall-normal plane from (a) D-M3 and (b) D-M6.

(1.10) is a good model for the eddy viscosity in the logarithmic region. Next we measure the damping function in the near-wall region according to

$$D = \left(\frac{\tau_w}{dU/dy} - \mu\right) \Big/ \left(\sqrt{\rho\rho_w}\kappa u_\tau y\right). \tag{3.1}$$

The results are shown in Figure 7(b) as functions of y_{SL}. The measured D is approximately 1 in the wall-normal distance range $40 < y_{SL} < 100$ in D-M3. This is consistent with Figure 7(a) and shows that Eq. (1.10) is a good approximation of the eddy viscosity in the logarithmic region. A logarithmic region is absent in case D-M6 because of the limited Reynolds number. Equation (1.5) under-estimates the wall damping effects, and conventional viscous scaling leads to an overly large damping function D. By contrast,

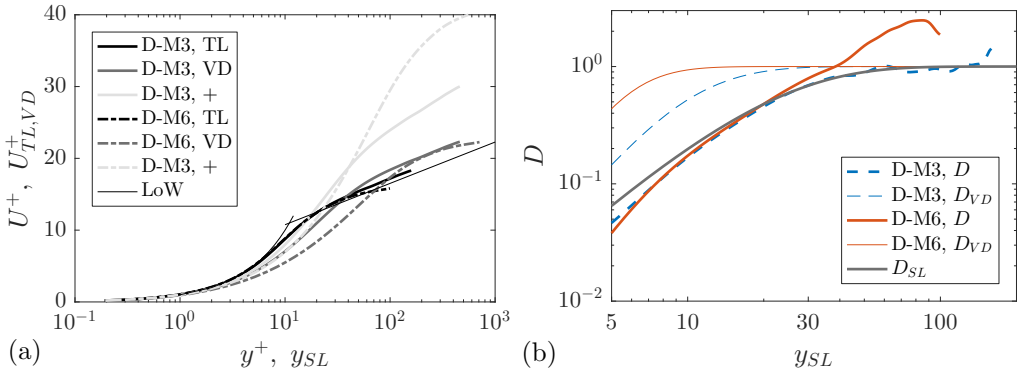

FIGURE 7. (a) The untransformed (U^+) and transformed ($U^+_{TL,VD}$) mean velocity profiles as functions of y^+ and y_{SL} on a log-linear scale. The incompressible law of the wall is indicated using thin lines, which consists of a linear region and a logarithmic region ($\kappa = 0.4$). Results of case D-M3 are shown using bold solid lines and results of case D-M3 are shown using bold dashed lines. (b) Damping function against y_{SL} on a log-log scale. The bold lines are DNS results. The thin lines correspond to Eq. (1.5) and the line in gray corresponds to Eq. (1.11).

Eq. (1.11) (i.e., using semi-local scaling in the damping function) seems to be a good model for the near-wall damping on the eddy viscosity. The DNS results are in favor of Eq. (1.11). This is consistent with the results in figures 2 and 3. The near-wall scaling of eddy viscosity was also investigated in Patel *et al.* (2016), but the focus was on the data collapsing using the semi-local scaling, and the effective Reynolds number was so limited in this work that a logarithmic region (a region where $D = 1$) can barely be found.

Equation (1.11) is supported by the DNS. Its usefulness in the context of WMLES is yet to be consolidated. Next, we compare WMLES with DNS. First, by comparing W-M3$_{\mathrm{VD,c}}$ and W-M3$_{\mathrm{VD,f}}$, W-M3$_{\mathrm{SL,c}}$ and W-M3$_{\mathrm{SL,f}}$, we conclude that WMLES results are grid converged (at least for typical WMLES grids). Second, the WMLES predicted wall-shear stresses are off by 63% and 127% for the wall Mach number $M_w = 3$ case and the $M_w = 6$ case, respectively, when using Eq. (1.5) as the damping function. Errors in wall-shear stress are often found in incompressible flow calculations, and are known as log layer mismatch (Kawai & Larsson 2012; Yang *et al.* 2017*a*). Log-layer mismatch, as discussed by Yang *et al.* (2017*a*); Kawai & Larsson (2012), if present, can only lead to a 15% error, but the error here is $> 50\%$. Hence we conclude that the problem identified here is new. Third, the error in wall-shear stress decreases to less than 5% when Eq. (1.11) is used. In addition to the zero-th order quantity (i.e., wall shear stress), a first order quantity, mean velocity profile, is examined in Figure 8. Because of the symmetry with respect to the channel center line, the mean velocity near the top wall is not shown for brevity. It is clear from Figure 8 that the disagreement between the WMLES and the DNS decreases when using Eq. (1.11) (as opposed to Eq. (1.5)). The disagreement in the bulk region may be due to deficiencies of the sub-grid model (see discussion in Yang & Bose 2017).

Because of the limited Reynolds number, the wall-model/LES matching locations are at distances fairly close to the wall: $y_{SL} = 14$ and $y_{SL} = 23$ in cases W-M3$_{\mathrm{SL,f}}$ and W-M6$_{\mathrm{SL}}$ (which correspond to $y^+ = 94$ and $y^+ = 61$), where the difference between the two damping functions is exaggerated (purposefully): at $h^+_{wm} = 94$, 61, $D \approx 1$ according to Eq. (1.5), whereas h_{wm} Eq. (1.11) leads to $D < 1$. Because the damping function is only non-unit in $y_{SL} \lesssim 40$, one might expect that any error due to the damping function

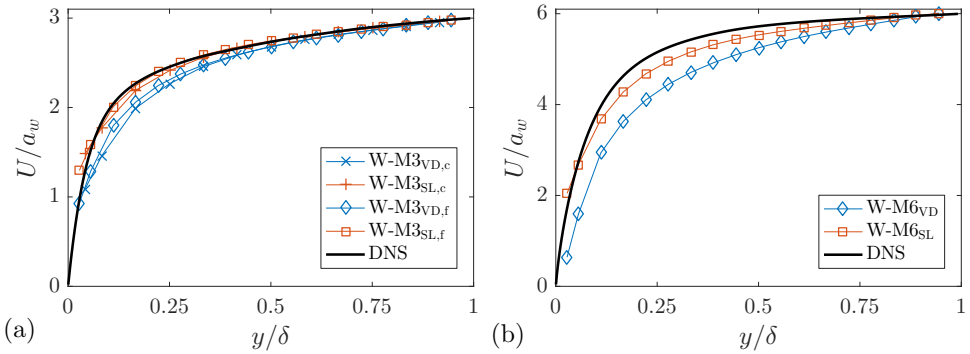

FIGURE 8. (a) Mean velocity as functions of the wall-normal coordinate. A frame of reference is chosen such that the wall is at rest. The wall Mach number is 3. The nomenclature of the WMLES cases are the same as in table 1. (b) Same as (a) but for $M_w = 6$.

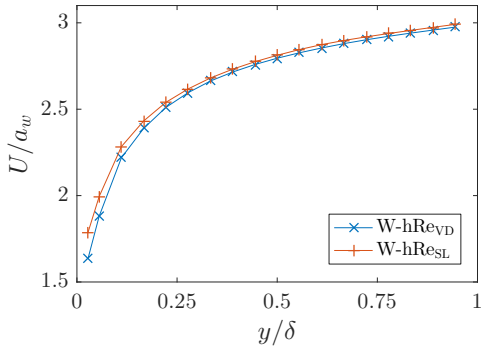

FIGURE 9. (a) Mean velocity profiles as functions of the wall-normal coordinate. A frame of reference is chosen such that the wall is at rest. The wall Mach number is 3. The nomenclature of the WMLES cases are the same as in Table 1.

will vanish at sufficiently high Reynolds numbers. Although it can be computationally costly to quantify this error as a function of Re^*_τ by comparing WMLES with DNS, we may still compare two WMLES, which use Eq. (1.5) and Eq. (1.11). By comparing W-hRe$_{\mathrm{VD}}$ and W-hRe$_{\mathrm{SL}}$, a 35% error in wall-shear stress is found at $Re^*_\tau \approx 6000$. The wall-model/LES matching locations are at $y_{SL} = 9.9\times10^2$, $y^+ = 2.8\times10^3$ and $y_{SL} = 8.6\times10^2$, $y^+ = 2.4\times10^3$ for W-hRe$_{\mathrm{VD}}$ and W-hRe$_{\mathrm{SL}}$, where the damping function D is already unit according to both Eq. (1.5) and Eq. (1.11). The error does decrease as a function of the Reynolds number, from 63% at $Re^*_\tau = 160$ to 35% at $Re^*_\tau \approx 6000$, but the decrease with Reynolds number is at most moderate. Figure 9 shows the mean velocity profiles as functions of the wall-normal coordinate. There is still notable difference between the two WMLES in the near-wall region.

Repeating this exercise at different Reynolds numbers is computationally costly even using the comparably cost-efficient WMLES. Here we solve Eqs. (1.2) and (1.3) using Eq. (1.5) and Eq. (1.11) for supersonic Couette flow at different Reynolds numbers and wall Mach numbers. Figure 10(a) shows the computed drag coefficient ($C_f = \tau_w/(0.5\rho_c M_w^2 a_w^2)$) as functions of Re^*_τ for $M_w = 1.5$, 3 and 6. Results of D-M3, D-M6, W-M3$_{SL,c}$, W-M3$_{SLf}$, W-M6$_{SL}$ and W-hRe$_{SL}$ are included for comparison. The thin boundary layer equations appear to be a good model for the supersonic Couette flow (even without including a wake region correction (Yang *et al.* 2016; Sadique *et al.* 2017)).

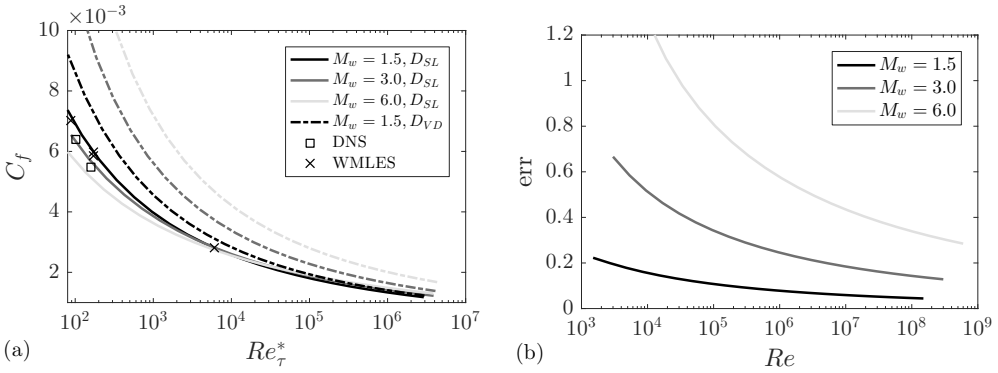

FIGURE 10. (a) Mean velocity profiles as functions of the wall-normal coordinate. A frame of reference is chosen such that the wall is at rest. The wall Mach number is 3. The nomenclature of the WMLES cases are the same as in table 1. (b) error in wall-shear stress when using Eq. (1.5) with respect to wall-shear stress predicted using Eq. (1.11).

Using Eq. (1.11) for the near-wall damping, the computed drag coefficient is only a weak function of the wall Mach number (this is expected), but using Eq. (1.5), the computed drag coefficient depends sensitively on the wall Mach number. The computed drag coefficients are less different at high Reynolds numbers when using Eq. (1.5) and Eq. (1.11). The difference between the wall-shear stresses is shown as functions of $Re = a_w M_w \rho_o / \mu_w$ in Figure 10 (b). The difference increases as a function of the wall Mach number (this is expected as the difference between the two damping functions are only notably different at high Mach numbers). For practically relevant Reynolds numbers ($Re \approx 10^7$) and flows at Mach number > 2, it is probably safe to conclude that Eq. (1.11) must be used in wall-modeled calculations, otherwise, a 30% error in wall-shear stress is to be expected.

4. Conclusions

The eddy viscosity in the logarithmic region is approximately $\mu_t = \sqrt{\rho \rho_w} \kappa u_\tau y$, which may be derived using the incompressible law of the wall and the van Driest transformation/the Trettel-Larsson transformation. Although the van Driest transformation fails for flows above non-adiabatic walls, the Trettel-Larsson transformation is found to work quite well at high speeds and for non-adiabatic walls. In the near-wall viscosity-affected region, a damping function needs to be used to account for the wall damping effects on the eddy viscosity. The empirically-determined damping function is $D = [1 - \exp(y/l_\nu/A^+)]^2$ for low-speed flows, where $l_\nu = \mu_w/(u_\tau \rho_w)$ and $A^+ = 17$. In the context of high speed flows, l_ν is $\mu_w/(u_\tau \rho_w)$ according to the van Driest transformation, and l_ν is $\mu/\sqrt{\rho \tau_w}$ according to the Trettel-Larsson transformation. Results in this work favors the semi-local scaling $l_\nu = \mu/\sqrt{\rho \tau_w}$. The WMLES predicted wall-shear stress will be off by $\approx 100\%$ at low Reynolds numbers and $\approx 30\%$ at high Reynolds numbers if the conventional viscous scaling is used for normalizing the wall-normal distance y in the damping function at high speeds. The error decreases to less than 5% when Eq. (1.11) is used. While the discussion of this work has focused on momentum transport, the usefulness of the semi-local scaling probably extends to energy transport (Patel *et al.* 2017). Compared to momentum transport, much less modeling work has been devoted to the turbulent energy transport in the near-wall region. In fact, the common practice is to simply invoke the Reynolds analogy and to take $\mathrm{Pr}_t = 0.9$ in the wall model, irrespective of the flow under consideration.

Although near-wall heat-transfer modeling is beyond the scope of this work, it would be useful to document formally the usefulness of the semi-local scaling for heat transfer problems at high speeds (Yang *et al.* 2017*b*).

Acknowledgments

This investigation is funded by AFOSR, Grant #1194592-1-TAAHO.

REFERENCES

Bermejo-Moreno, I., Campo, L., Larsson, J., Bodart, J., Helmer, D. & Eaton, J. K. 2014 Confinement effects in shock wave/turbulent boundary layer interactions through wall-modeled large-eddy simulations. *J. Fluid Mech.* **758**, 5–62.

Bermejo-Moreno, I., Larsson, J., Campo, L., Bodart, J., Vicquelin, R., Helmer, D. & Eaton, J. 2011 Wall-modeled large eddy simulation of shock/turbulent boundary-layer interaction in a duct. *Annual Research Briefs* pp. 49–62.

Bhagatwala, A. & Lele, S. K. 2009 A modified artificial viscosity approach for compressible turbulence simulations. *J. Comput. Phys.* **228**, 4965–4969.

Choi, H. & Moin, P. 2012 Grid-point requirements for large eddy simulation: Chapman's estimates revisited. *Phys. Fluids* **24**, 011702.

Coleman, G. N., Kim, J. & Moser, R. 1995 A numerical study of turbulent supersonic isothermal-wall channel flow. *J. Fluid Mech.* **305**, 159–183.

Ducros, F., Ferrand, V., Nicoud, F., Weber, C., Darracq, D., Gacherieu, C. & Poinsot, T. 1999 Large-eddy simulation of the shock/turbulence interaction. *J. Comput. Phys.* **152**, 517–549.

Foysi, H., Sarkar, S. & Friedrich, R. 2004 Compressibility effects and turbulence scalings in supersonic channel flow. *J. Fluid Mech.* **509**, 207–216.

Guarini, S. E., Moser, R. D., Shariff, K. & Wray, A. 2000 Direct numerical simulation of a supersonic turbulent boundary layer at Mach 2.5. *J. Fluid Mech.* **414**, 1–33.

Hoyas, S. & Jiménez, J. 2006 Scaling of the velocity fluctuations in turbulent channels up to $\mathrm{Re}_\tau = 2003$. *Phys. Fluids* **18**, 011702.

Huang, P. G., Coleman, G. N. & Bradshaw, P. 1995 Compressible turbulent channel flows: DNS results and modelling. *J. Fluid Mech.* **305**, 185–218.

Joo, J., Medic, G., Philips, D. & Bose, S. 2014 Large-eddy simulation of a compressor rotor. *Proceedings of the Summer Program,* Center for Turbulence Research, Stanford University, pp. 467-477.

Kawai, S. & Asada, K. 2013 Wall-modeled large-eddy simulation of high Reynolds number flow around an airfoil near stall condition. *Comput. Fluids* **85**, 105–113.

Kawai, S. & Larsson, J. 2012 Wall-modeling in large eddy simulation: Length scales, grid resolution, and accuracy. *Phys. Fluids* **24**, 015105.

Khalighi, Y., Nichols, J. W., Lele, S., Ham, F. & Moin, P. 2011 Unstructured large eddy simulation for prediction of noise issued from turbulent jets in various configurations. *AIAA Paper* #2011-2886.

Larsson, J., Kawai, S., Bodart, J. & Bermejo-Moreno, I. 2016 Large eddy sim-

ulation with modeled wall-stress: recent progress and future directions. *Mech. Eng. Rev.* **3**, 15–00418.

Larsson, J., Laurence, S., Bermejo-Moreno, I., Bodart, J., Karl, S. & Vicquelin, R. 2015 Incipient thermal choking and stable shock-train formation in the heat-release region of a scramjet combustor. part II: Large eddy simulations. *Combust. Flame* **162**, 907–920.

Lee, M. & Moser, R. D. 2015 Direct numerical simulation of turbulent channel flow up to $\mathrm{Re}_\tau \approx 5200$. *J. Fluid Mech.* **774**, 395–415.

Lozano-Durán, A. & Jiménez, J. 2014 Effect of the computational domain on direct simulations of turbulent channels up to $\mathrm{Re}_\tau = 4200$. *Phys. Fluids* **26**, 011702.

Martín, M. P. 2007 Direct numerical simulation of hypersonic turbulent boundary layers. Part 1. initialization and comparison with experiments. *J. Fluid Mech.* **570**, 347–364.

Marusic, I., Monty, J. P., Hultmark, M. & Smits, A. J. 2013 On the logarithmic region in wall turbulence. *J. Fluid Mech.* **716**, R3.

Park, G. I. 2017 Wall-modeled large-eddy simulation of a high Reynolds number separating and reattaching flow. *AIAA J.* **55**, 3709-3721.

Park, G. I. & Moin, P. 2014 An improved dynamic non-equilibrium wall-model for large eddy simulation. *Phys. Fluids* **26**, 015108.

Patel, A., Boersma, B. J. & Pecnik, R. 2016 The influence of near-wall density and viscosity gradients on turbulence in channel flows. *J. Fluid Mech.* **809**, 793–820.

Patel, A., Boersma, B. J. & Pecnik, R. 2017 Scalar statistics in variable property turbulent channel flows. *Phys. Rev. Fluids* **2**, 084604.

Patel, A., Peeters, J. W., Boersma, B. J. & Pecnik, R. 2015 Semi-local scaling and turbulence modulation in variable property turbulent channel flows. *Phys. Fluids* **27**, 095101.

Piomelli, U. 2008 Wall-layer models for large-eddy simulations. *Prog. Aerosp. Sci.* **44**, 437–446.

Piomelli, U. & Balaras, E. 2002 Wall-layer models for large-eddy simulations. *Annu. Rev. Fluid Mech.* **34**, 349–374.

Pirozzoli, S. & Bernardini, M. 2013 Probing high-Reynolds-number effects in numerical boundary layers. *Phys. Fluids* **25**, 021704.

Pope, S. B. 2001 *Turbulent Flows.* Cambridge University Press.

Sadique, J., Yang, X. I. A., Meneveau, C. & Mittal, R. 2017 Aerodynamic properties of rough surfaces with high aspect-ratio roughness elements: Effect of aspect ratio and arrangements. *Boundary-Layer Meteorol.* **163**, 203–224.

Trettel, A. & Larsson, J. 2016 Mean velocity scaling for compressible wall turbulence with heat transfer. *Phys. Fluids* **28**, 026102.

van Driest, E. R. 2003 Turbulent boundary layer in compressible fluids. *J. Spacecraft Rockets* **40**, 1012–1028.

Yang, X. I. A., Sadique, J., Mittal, R. & Meneveau, C. 2016 Exponential roughness layer and analytical model for turbulent boundary layer flow over rectangular-prism roughness elements. *J. Fluid Mech.* **789**, 127–165.

Yang, X. I. A. & Bose, S. T. 2017 A physical basis of the slip-wall model for wall-modeled large-eddy simulations. In *10th International Symposium on Turbulence and Shear Flow Phenomena (TSFP10).*

Yang, X. I. A. & Meneveau, C. 2016 Recycling inflow method for simulations of

spatially evolving turbulent boundary layers over rough surfaces. *J. Turbul.* **17**, 75–93.

Yang, X. I. A., Park, G. I. & Moin, P. 2017*a* Log-layer mismatch and modeling of the fluctuating wall stress in wall-modeled large-eddy simulations. *Phys. Rev. Fluids* **2**, 104601.

Yang, X. I. A., Sadique, J., Mittal, R. & Meneveau, C. 2015 Integral wall model for large eddy simulations of wall-bounded turbulent flows. *Phys. Fluids* **27**, 025112.

Yang, X. I. A., Urzay, J., Bose, S. & Moin, P. 2017*b* Aerodynamic heating in wall-modeled LES of high-speed flows. *AIAA J.* (In Press), doi: 10.2514/1.J056240.

You, D. & Moin, P. 2007 A dynamic global-coefficient subgrid-scale eddy-viscosity model for large-eddy simulation in complex geometries. *Phys. Fluids* **19**, 065110.